Journal of the Brazilian Society of Mechanical Sciences and Engineering (2024) 46:346
https://doi.org/10.1007/s40430-024-04942-7

TECHNICAL PAPER

Research on performance failure caused by gas blocking in multiphase mixed-transport pump under non-uniform inflow conditions

Hui Quan[1] · Zhisheng Wang[1] · Yuanying Du[1] · Houde Su[2]

Received: 27 October 2023 / Accepted: 22 April 2024 / Published online: 9 May 2024

Abstract

The helical–axial multiphase mixed-transport pump fails due to gas blocking caused by gas–liquid separation caused by cavitation under complex conditions with high gas volume fraction. This is an urgent engineering problem that needs to be addressed in the application of this pump. In order to simulate the flow structure characteristics in the channel, two types of non-uniform inflow boundary conditions are introduced. The bubble structure, velocity, and pressure of the inflow conditions under different operating conditions are compared and analyzed, and the variation rules affected by the non-uniform boundary conditions are obtained. At the same time, the internal flow characteristics and mechanisms of helical–axial multiphase mixed-transport pump are analyzed based on the velocity changes at the inlet of the impeller and the pressure fluctuations at the outlet of the diffuser, leading to the intensification of gas–liquid separation and eventually the development of gas blocking. Research has shown that by changing the flow boundary conditions through the UDF program, it has been found that the linear change in inlet pressure has a more pronounced effect on the gas–liquid separation in the flow channel of the mixed-transport pump than the sinusoidal change, leading to a serious decline in pump performance when gas blocking occurs, until failure. When the inlet gas content is 10%, with the increase in flow rate, the head of the linear boundary condition decreases significantly at 0.95 Q/Qd Along the axial direction of the flow channel, the velocity disturbance of the linear boundary condition is significant on the suction surface of the blade, and the low-pressure area inside the flow channel is 30% higher than that of the sinusoidal boundary condition. The research conclusion can provide reference value for solving the problem of gas blocking in engineering applications of helical–axial multiphase mixed-transport pump.

Keywords Helical–axial multiphase mixed-transport pump · Non-uniform inflow · Bubble structure · Gas blocking phenomenon · Visualization experiment

1 Introduction

In the span of the last few decades, there has been a marked and continuous growth in the development and extraction activities of oil and gas fields, both offshore and terrestrial. The complex amalgam of substances, including oil, gas, water, and a variety of impurities that are drawn directly from oil wells, requires consolidated transportation to various processing sites. Accordingly, the refined methodologies in mixed oil and gas transportation, epitomized by the advanced helical–axial multiphase mixed-transport pumps, have increasingly become the focal point of academic and industrial research [1]. Quan Hui et al. [2] observed that the asynchronous behavior of gas–liquid two-phase media, resulting in gas–liquid separation, stands as the primary cause for the malfunction of helical–axial multiphase mixed-transport pumps in engineering applications, which can precipitate damage to the pumps or render them inoperable.

Previously, researchers have extensively investigated the impact of inflow boundary conditions on the functioning, acoustical vibrations, and inner flow dynamics of single-phase pump systems. Murakami et al. [3] conducted experiments and analysis on the hydraulic performance of a horizontal centrifugal pump equipped with a curved inlet pipe, and discovered that the velocity distribution at the impeller's entrance was non-uniform. The secondary flow induced by

Technical Editor: Erick Franklin.

✉ Zhisheng Wang
wangzs@lut.edu.cn

[1] College of Energy and Power Engineering, Lanzhou University of Technology, Lanzhou 730050, China

[2] Lanpec Technologies Limited, Lanzhou 730070, China

the bend at the inlet and the rotational flow generated by the pump impeller combine. This interaction results in an increased fluid velocity in the vicinity of the elbow of the inlet pipe, whereas the fluid velocity decreases further away from the elbow [4]. Cao et al. [5] investigated the influence of non-uniform inflow on the efficiency of water jet propulsion pumps and observed that the irregularity at the inlet resulted in a considerable reduction of the pump's head. Luo et al. [6] delved into the underlying causes and mechanisms behind energy dissipation and pressure instability stemming from the irregular inflow in water jet propulsion pumps. Uncovering that non-uniform inflow can diminish head and efficiency, and amplify axial force variations on the impeller, thus resulting in pronounced fluctuations in the non-steady-state energy performance. Yuan et al. [7] discovered that an uneven inlet flow, often induced by elbow structures, constitutes a significant factor in the reduced energy transformation efficiency of centrifugal pumps. His prototype experiments on centrifugal pumps revealed the differences in energy conversion characteristics between uniform and non-uniform elbow inflows. It was observed that an uneven elbow inflow elevates hydraulic losses within the centrifugal pump, which in turn lowers the pump head and operational efficiency, leading to an efficiency reduction of up to 8% under designated flow conditions. Advanced simulations using a viscous modified shear-stress transport (SST) large eddy simulation model were employed to examine the flow excitation properties and energy evolution patterns. The results highlighted that non-uniform inflow heightens shock losses at the impeller's entrance and instigates unsteady flow excitation within the impeller passages.

Zheng Xiaolong et al. [8] ascertained that the flow field's non-uniformity predominantly contributes to the prominence of low-frequency discrete noise over high-frequency noise within the propeller's acoustic field. As frequency rises, the rate of noise attenuation tends to decline. Moreover, both axial and radial noise attenuation velocities diminish as the distance from the propeller disk's center increases, with the axial sound pressure levels being notably lower in comparison to the radial directions on either side. Liu Liyun et al. [9] independently devised a sophisticated hydrodynamic analysis and acoustic prediction platform tailored for underwater propellers, which is built upon Open FOAM and the Ffowcs Williams-Hawkings (FW-H) acoustic analogy approach. They implemented a permeable surface as the integral boundary to enable the computation of noise stemming from nonlinear acoustic sources. It was recognized that the nonlinear noise source term of the propeller is of substantial importance and should not be overlooked. Huang et al. [10] discovered that the manifestation of cavitation within water jet propulsion pumps results in significant fluctuations in the fluid dynamics, resulting in an irregular distribution of flow at the impeller inlet and compromised flow perpendicularity. Jian et al. [11] revealed that variations in the inlet's uniformity notably affect the fuel mixing process. Through a comparative analysis of the flow field dynamics between non-uniform and uniform flows, it was determined that the discrepancy in total pressure loss with non-uniform flow exceeds 4%, and the interior mixing coefficient within the cavity stands at merely 81% of that associated with a uniform flow. Zhang Liping [12] conducted an in-depth analysis of the pressure pulsation patterns in axial flow pumps subjected to varying inflow scenarios. His findings indicated that pressure pulsations under conditions of linear non-uniform inflow primarily stem from the interaction between the impeller and the diffuser. In contrast, with suction non-uniform inflow, the pulsations are predominantly driven by the irregularity of the inflow itself. The focus of the study is on the mechanistic impact that non-uniform edge boundary conditions exert on the external characteristics of mixed-flow transport pumps and on the internal flow structures within the channel, particularly under gas–liquid two-phase flow conditions.

Dating back to the latter half of the previous century, Yokoyama Shibata undertook empirical studies to scrutinize the influence of water temperature on the cavitation characteristics of centrifugal pumps. Through observations of air content and the bubble dynamics induced by the cavitation process, Shibata meticulously tracked the occurrence of cavitation within the impeller region. Furthermore, he explored how variations in water temperature, specifically within a low-temperature spectrum, could affect the cavitation behavior and efficiency of centrifugal pumps [13]. Zhang et al. [14] executed two simulations by varying the inlet pressure of the pump: one simulation depicted a scenario free of air cavities, while the other incorporated air pockets. The detection of cavitation phenomena revealed that the TLV (thermodynamic vapor lock) core trajectory shifted further from the pump's suction surface and approached the blade's upstream end wall. Within the cavitation regime, there was a notable decrease in eddy current velocity and turbulent kinetic energy, accompanied by a more pronounced pressure pulsation. This accumulation of bubbles within the electric submersible pump (ESP) during gas–liquid multiphase flow led to a spectrum of performance impairments, from marginal declines to the severe gas lock condition. Ali et al. [15] formulated an empirical model designed to forecast the hydraulic head and surge dynamics, and upon comparison with experimental results, discovered that it was both effective and broadly applicable in predicting the multiphase performance of pumps. Yuan et al. [16] analyzed the cavitation phenomenon occurring at the pump turbine's tongue in pump mode. The performance decline attributed to cavitation can be categorized into three stages correlating with its progression: bubbly cavitation, cloudy cavitation, and supercavitation. Al Obaidi et al. [17]

employed a proprietary model to examine the variations in pressure fluctuations of centrifugal pumps operating under single-phase and cavitation conditions across various discharge impeller diameter ranges (200, 210, and 220 mm). It was observed that the 210 mm volute exhibited an average pressure fluctuation approximately 6.74% greater than the 200 mm volute, while the 220 mm volute's maximum pressure fluctuation was about 7.4% higher compared to the 210 mm volute. Al Obaidi et al. [18, 19] investigated the mixed-flow dynamics of axial flow pumps across five operational scenarios, spanning from the best efficiency point (1.0 BEP) to an increased flow rate of 20 L per minute beyond the BEP. Furthermore, blade angles of − 3°, 0°, and 3° were examined, revealing that an escalation in blade angle correlates with heightened flow instability and pressure pulsations. Additionally, augmentation of the diffuser was found to notably influence both the flow field and the overall performance of the pump. Penteado et al. [20, 21] employed a drift flux model to capture the dynamics of gas–liquid flow within a centrifugal field, incorporating empirical data pertaining to bubble diameter, trajectory, and velocity, collated via high-speed photography across varied rotational velocities and rates of gas mass flow. This was part of an experimental examination of the two-phase flow properties within a centrifugal pump.

The heterogeneity at the pump inlet due to gas–liquid separation is a crucial factor impacting the efficiency of multiphase mixed-flow transport pump. This uneven inflow, resulting from gas–liquid separation, predisposes the pump to gas block and operational failures, with the influence of such non-uniformity on two-phase flow pump not being sufficiently understood. Consequently, this study focuses on the helical–axial multiphase mixed-transport pump, utilizing a user-defined function (UDF) program to characterize the structural features of the non-uniform inflow under gas–liquid biphasic conditions, and to quantify its effects on the pump's operational characteristics. Through a synergy of numerical simulations and visual experiments, this article delves into the distribution traits and the developmental mechanism of the gas–liquid two-phase flow structure under skewed inflow conditions, laying a groundwork for future industrial production and engineering implementations.

2 Establishment of a model for helical–axial flow multiphase mixed-transport pump

2.1 Hydraulic design and 3D modeling

The main design parameters of a helical–axial multiphase mixed-transport pump (hereinafter referred to as a mixed-transport pump) with a specific speed of $n_s = 289.455$ a design flow rate of $Q\mathrm{d} = 100\,\mathrm{m}^3/\mathrm{h}$, a design speed of $n = 4500$ rpm, and a head of $H = 25$ m are shown in Table 1.

Table 1 Geometric parameters of impeller and diffuser

Basic parameters	Parameter value
Impeller outlet diameter D_2 (mm)	140
Hub inlet diameter d_{h1} (mm)	100
Hub outlet diameter d_{h2} (mm)	110
Number of impeller blades Z_v (piece)	4
Number of diffusers Z_b (piece)	13
Head coefficient Ψ_i	0.18
Rim diameter ratio S_L	0.32
Rim diameter D_i (mm)	142
Foliage density σ	2
Flow coefficient φ_i	0.107
Axial length of impeller e (mm)	138

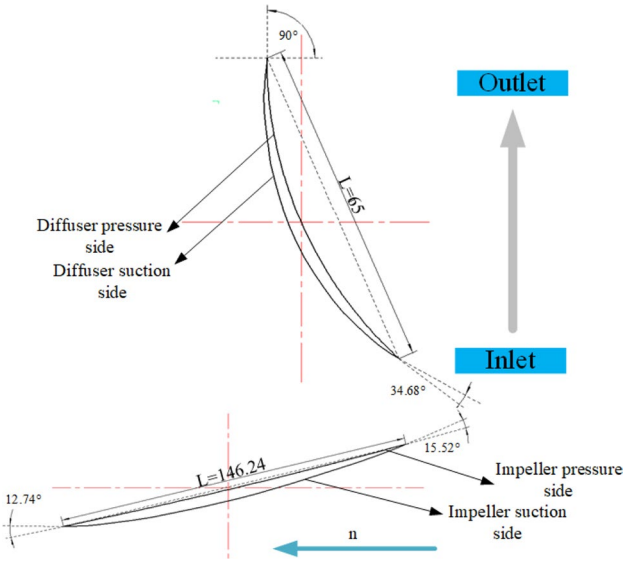

Fig. 1 Hydraulic design

Utilizing the geometric parameters detailed in Table 1, a two-dimensional axial view of the impeller and diffuser was created. As depicted in Fig. 1, this illustration presents an axial projection of a cross section that encompasses both the pressure and suction sides of the impeller and diffuser. The impeller is shown to rotate from right to left, with the fluid entering from the bottom and exiting at the top. A computational fluid domain was formulated based on the hydraulic design in Fig. 1, primarily incorporating the inlet section, impeller, diffuser, and outlet section. Key elements of the mixed-flow transport pump were fashioned in three dimensions using the Creo 7.0 software, as evident in Fig. 2. To facilitate the complete establishment of the flow at the inlet and outlet boundaries, their lengths were extended to 1.5

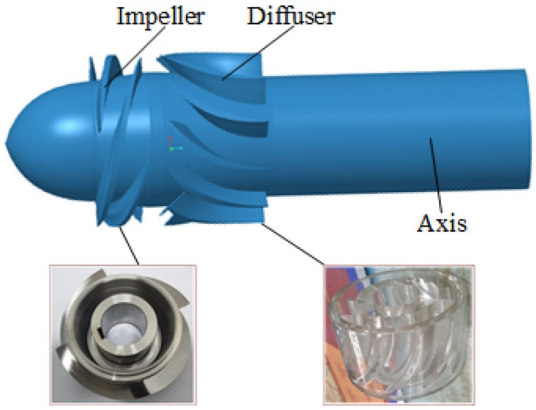

Fig. 2 Model of mixed-transport pump

and 2.5 times the diameter of the pipe correspondingly. For the purpose of simplifying the experimentation on flow field visualization, the diffuser and housing were crafted from transparent polymethyl methacrylate (PMMA) organic glass, and the resultant physical model is exhibited in Fig. 2.

2.2 Grid partitioning and independence testing

During the simulation process in Fluent, it has been observed that polyhedral meshes within an unstructured mesh framework offer superior geometric conformity and computational convergence. Initially, the computational domain is subjected to tetrahedral meshing using Workbench Mesh, with subsequent refinement via an expansion algorithm applied specifically to the impeller, diffuser, and the junctions of inlet and outlet. Additionally, a local refinement is conducted on the blade to generate the preliminary mesh structure. The tetrahedral mesh, once drafted, is then imported into Fluent where it is transformed into a polyhedral mesh, as illustrated in Fig. 3. This method yields five distinct polyhedral meshes, which are then subjected to a mesh independence validation to ensure accuracy and reliability of the simulation results.

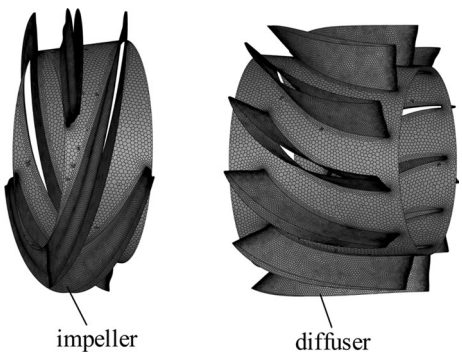

Fig. 3 Polyhedral mesh

Following the simulations, it has been observed that with an incremental rise in the mesh count, there is a corresponding increase in both the head and efficiency of the mixed-flow transport pump, which gradually approaches a state of stability. The performance parameters of the pump demonstrate negligible variance between the fourth and fifth mesh configurations, indicating that the discrepancies in the numerical simulation outcomes from these iterations are marginal and can be disregarded. In balancing computational resources and efficiency, the fourth grid configuration was selected for further investigation. The final tally of unstructured meshes within the computational domain amounts to 7,886,802, and the results of the mesh independence test are depicted in Fig. 4.

3 Theoretical analysis of multiphase flow cavitation model

3.1 Establishment of control equations

The Mixture model for multiphase flow is employed to simulate the cavitation phenomena within multiphase pump. For the turbulence closure, the standard k-ε model is utilized. When addressing turbulence in the vicinity of walls, the standard wall function approach is applied. This methodology is apt for scenarios involving phase mixing or separation within the flow field, or in instances where the volume fraction of the dispersed phase is in excess of 10%. Within Fluent, the governing equations of the Mixture model predominantly comprise the continuity, momentum, and energy equations for the mixture, which are formulated as follows [22, 23]

Continuity equation: the continuity equation of the mixture is

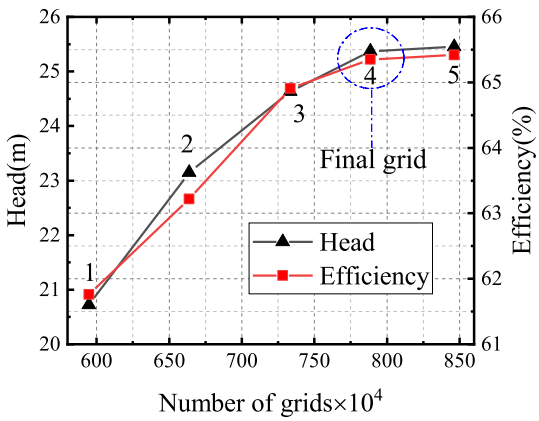

Fig. 4 Grid independence verification

$$\frac{\partial \rho_{\mathrm{m}}}{\partial t}+\nabla \cdot\left(\rho_{\mathrm{m}} u_{\mathrm{m}}\right)=0 \tag{1}$$

In the formula: ρ_{m} is the density of the mixture; u_{m} is the average speed of mass.

Momentum equation. The momentum equation of the Mixture model can be obtained by summing the momentum equations of all phases, and for incompressible fluids, it can be expressed as

$$\frac{\partial\left(\rho_{\mathrm{m}} u_{\mathrm{m}}\right)}{\partial t}+\nabla \cdot\left(\rho_{\mathrm{m}} u_{\mathrm{m}} u_{\mathrm{m}}\right)=-\nabla p+\nabla \cdot\left[\mu_{\mathrm{m}}\left(\nabla u_{\mathrm{m}}+\nabla u_{\mathrm{m}}^{T}\right)\right]+\rho_{\mathrm{m}} g+F-\nabla \cdot\left(\rho_{\mathrm{m}} u_{\mathrm{m}}, 0\right) \tag{2}$$

In the formula: g is the acceleration of gravity; F is physical strength; u_m is the viscosity of hybrid power.

Energy equation. The energy equation of the mixture is as follows:

$$\frac{\partial}{\partial_t} \sum_{k=1}^{n}\left(\alpha_k \rho_k E_k\right)+\nabla \cdot \sum_{k=1}^{n}\left[\alpha_k u_k\left(\rho_k E_k+p\right)\right]=\nabla \cdot\left(k_{\mathrm{eff}} \nabla T\right)+S_{\mathrm{E}} \tag{3}$$

In the formula, k_{eff} is the effective thermal conductivity, where k_{t} is the turbulent thermal conductivity coefficient. The first item on the right represents the energy transfer caused by conduction. S_{E} includes all other heat source energy.

3.2 Cavitation model

To characterize the mass transfer dynamics during phase transitions in cavitating flows, a cavitation model rooted in the Rayleigh–Plesset equation is applied. This equation offers insight into the dynamic behavior of cavitation bubbles, detailing the rate at which they expand or collapse in response to the variances between internal and external pressures. Notably, this model sets aside considerations related to heat conduction and non-equilibrium phase transition effects, and it adopts the method of component transport to articulate the transport equation for the vapor volume fraction, which is described as follows [24].

$$\frac{\partial\left(\rho_v \alpha_{\mathrm{v}}\right)}{\partial_t}+\nabla \cdot\left(\rho_v \alpha_{\mathrm{v}} u\right)=\dot{m}^{+}-\dot{m}^{-} \tag{4}$$

In the formula: α_{v} is the volume fraction of the vapor phase; α_{v} is the vapor phase density; u is the velocity of the mixed fluid; $\dot{m}^{+}$ is the rate of fluid evaporation; and $\dot{m}^{+}$ is the rate of fluid condensation.

In order to construct $\dot{m}^{+}$ and $\dot{m}^{-}$, the Rayleigh–Plesset equation is introduced to describe the bubble dynamics equation of a cavitation bubble, which describes the volume expansion or collapse velocity of a cavitation bubble under the action of internal and external pressure differences. Its form is

$$R_{\mathrm{B}} \frac{\mathrm{d}^2 R_{\mathrm{B}}}{\mathrm{d}t^2}+\frac{3}{2}\left(\frac{\mathrm{d}R_{\mathrm{B}}}{d_t}\right)^2=\left(\frac{p_{\mathrm{v}}-p}{\rho_{\mathrm{l}}}\right)-\frac{4 v_{\mathrm{l}}}{R_{\mathrm{B}}} \frac{\mathrm{d}R_{\mathrm{B}}}{d_t}-\frac{2S}{\rho_{\mathrm{l}} R_{\mathrm{B}}} \tag{5}$$

In the formula: R_{B} is the radius of the bubble; p_v is the pressure inside the cavity (saturated vapor pressure at ambient temperature); p is the liquid pressure; v_{l} is the kinematic viscosity of the liquid; S is the surface tension coefficient; and ρ_{l} is the density of the liquid.

Ignoring the effects of second-order terms, surface tension, fluid viscosity, and non-condensable gas, the relationship between changes in bubble radius and pressure can be obtained:

$$\frac{\mathrm{d}R_{\mathrm{B}}}{\mathrm{d}t}=\pm \sqrt{\frac{2}{3} \frac{\left|p_{\mathrm{v}}-p\right|}{\rho_{\mathrm{l}}}} \tag{6}$$

The Zwart–Gerber–Belamri model was proposed by Zwart which assumes that all bubbles in the system are of the same size [25]. The mass transfer rate per unit volume is calculated using the density of bubbles and the rate of change per unit mass:

$$\dot{m}=n_{\mathrm{b}}\left(4 \pi R_{\mathrm{B}}^2 \rho_{\mathrm{v}} \frac{\mathrm{d}R_{\mathrm{B}}}{dt}\right) \tag{7}$$

In the formula: n_{b} is the density of bubbles.

There is a relationship between the void number density and the vapor phase volume fraction, as well as the void radius, as follows

$$\alpha_{\mathrm{v}}=n_{\mathrm{b}}\left(\frac{4}{3} \pi R_{\mathrm{B}}^3\right) \tag{8}$$

Then, Eq. (7) becomes

$$\dot{m}=\frac{3 \alpha_{\mathrm{v}} \rho_{\mathrm{v}}}{R_{\mathrm{B}}} \sqrt{\frac{2}{3} \frac{p_{\mathrm{v}}-p}{\rho_{\mathrm{l}}}} \tag{9}$$

From Eq. (9), it can be obtained that the main part of the interphase mass transfer rate (the left part of the root sign) is only related to the vapor phase density, and is not related to the liquid phase density. In order to solve the problem that Eq. (13) only applies to the initial stage of cavitation and the density of cavitation nucleons inevitably decreases with the increase in vapor volume fraction, Zwart et al. proposed using $\alpha_{\mathrm{nuc}}\left(1-\alpha_{\mathrm{v}}\right)$ instead of α_{v}

$$m^{+} = F_{\mathrm{vap}} \frac{3\alpha_{\mathrm{nuc}}\left(1-\alpha_{\mathrm{v}}\right)\rho_{\mathrm{v}}}{R_{\mathrm{B}}} \sqrt{\frac{2}{3}\frac{p_{\mathrm{v}}-p}{\rho_{\mathrm{l}}}} \quad p \le p_{\mathrm{v}} \tag{10}$$

$$m^{-} = F_{\mathrm{cond}} \frac{3\alpha_{\mathrm{v}}\rho_{\mathrm{v}}}{R_{\mathrm{B}}} \sqrt{\frac{2}{3}\frac{p_{\mathrm{v}}-p}{\rho_{\mathrm{l}}}} \quad p > p_{\mathrm{v}} \tag{11}$$

In the formula: α_{nuc} is the volume fraction of cavitation nucleons, taken as $5\times10-4$; F_{vap} is the evaporation coefficient, which is an empirical constant used to correct the evaporation calculation results. In this simulation, 50 is taken; F_{cond} is the condensation coefficient and is also an empirical constant, taken as 0.01. The bubble radius is taken as $R_{\mathrm{B}} = 1\times10^{-6}$m.

3.3 Boundary

In this paper, considering the calculation cost and accuracy, Reynolds time average Navier–Stokes equation and k-ε turbulence model are used to numerically simulate the helical–axial multiphase mixed-transport pump. The convergence accuracy is set to 1.0×10^{-4}, the transient calculation is monitored once every 1°, and the time step is 3.7×10^{-5} s. The density of normal temperature water used in the initial fluid is 1050 kg/m^3, the viscosity is 2.98×10^{-3} Pa s, and the saturated steam pressure Pv = 3574 Pa. The pressure inlet is controlled by Eqs. 12 and 13, and the mass flow at the outlet is set to 27.78 kg/s. The phase volume fraction of inlet breath is set to 10%. The wall boundary conditions are set to non-slip wall and adiabatic wall. By reducing the total inlet pressure value, the cavitation process simulates the development of the bubble in three main stages.

4 Test methods

To validate the precision of the numerical simulations and to elucidate the principles behind bubble formation and flow patterns within the pump, our research group established a test rig for a helical–axial multiphase mixed-transport pump, as illustrated in Fig. 5. Quan et al. [26] conducted an analysis of the internal flow structure within a helical–axial multiphase pump during water transportation through a series of experiments. Through experimental analysis, it was observed that higher liquid viscosity leads to an increase in velocity vectors close to both the rim and the hub of the wheel, as well as an escalation in turbulent kinetic energy in these zones. This heightened turbulence contributes to increased flow losses. Consequently, the impeller's capacity to enhance pressure is compromised, leading to a reduction in pump head. Additionally, the study explored the impact of various flow fields on the pump's energy conversion efficiency. It was noted that within the impeller, the point of gas–liquid separation typically occurs at approximately two-thirds along the chord of the blade. The separation process results in the formation of gas pockets, which can lead to gas blockage and subsequent energy losses within the compression section.

In this study, comprehensive testing of the pump's external characteristics was performed under varying gas content conditions. First, the pump was stabilized at a predefined flow rate. Based on the designated inflow requirements, the gas content was then calculated, and the volume fraction of gas entering the gas–liquid mixer was meticulously controlled by adjusting the valve on the gas line. Thanks to the precision of electromagnetic and vortex flowmeters used, the uncertainty in the measured gas content was gauged to be as minimal as 0.005%. For the visualization experiments, it was crucial to position the test pump's axial direction so that it was orthogonal to the camera's line of light, effectively minimizing angle-related errors due to inconsistent

Fig. 5 Visual experiment system

viewing perspectives. To ensure maximum clarity in the captured images, the experiments were preferably carried out at night time, using additional lighting sources to enhance the contrast between the focus area and its surroundings. The camera setup was carefully adjusted, fine-tuning the distance and focus of the lens for optimal image capture. High-speed imagery was acquired using a dynamic camera, recording at a remarkable rate of 10,000 frames per second. The resulting images boasted a high resolution of 1920×1080 pixels, with an impressively short exposure time of 30 microseconds. This setup allowed for an intricate observation of the gas–liquid biphasic movement within the flow field, as depicted in Fig. 5 of the high-speed camera experiment setup.

Utilizing a synergy between MATLAB software and precision measuring instruments, the study captured the pressure and torque data from sensors at both the pump's inlet and outlet under a variety of inflow conditions. This approach enabled the calculation of the external characteristic curve for the mixed-flow pump at an inlet gas content of 10%. The ensuing curve, along with its comparison with numerical simulations, is presented in Fig. 6. Examination of the graph reveals that the discrepancies between the simulated and experimental results stay below a 5% margin of error, thereby affirming the numerical simulation's credibility.

5 Implementation of non-uniform inflow

In practical engineering scenarios, attaining a uniform flow at the water pump inlet is often challenging. To investigate the impact of such non-uniform inflow on a helical–axial multiphase mixed-transport pump, the study entails calculating non-uniform boundary conditions for pressure as outlined in Eqs. (12) and (13). These calculations were executed using the C programming language

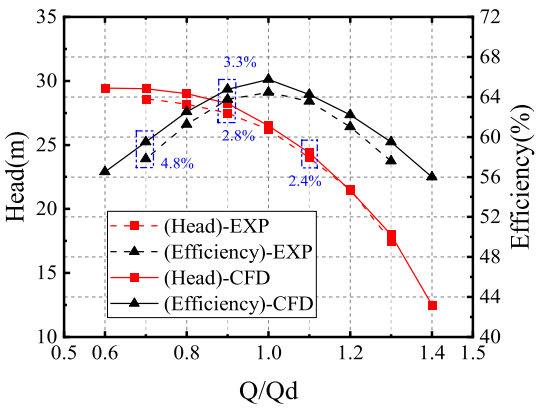

Fig. 6 Experimental out-of-pump characteristic curve

and introduced into the pump's inlet boundary via a user-defined function (UDF) in the Fluent computational fluid dynamics software [27]. In the analysis of non-uniform inflow conditions, the study incorporates a straight pipe section preceding the impeller inlet to exert a comprehensive influence on the flow within the impeller region. This setup is depicted in Fig. 7, where the pressure distribution across the non-uniform leading surface is illustrated. The combined effects of the downward gravity along the y-axis and the disturbances within the internal flow contribute to a state where the inflow to the mixed-transport pump does not adhere to the principle of homogenous axial vectors during operation. The paper defines and implements two distinct non-uniform inlet boundary conditions as outlined in reference [12], to accurately emulate the suboptimal inflow scenarios encountered in pump operations. These conditions are constructed to reflect the reality of the operational environment, ensuring that the simulation accurately mimics the intricacies of pump performance under real-world conditions.

This article studies non-uniform inflow, taking the working condition with a gas content of 10% as an example, and calculates a critical cavitation pressure of 34000 pa at the onset of cavitation. The pressure obtained by integrating radially on the yoz plane is equal, reducing the error of numerical simulation. For non-uniform inflow I, the pressure distribution curve on the yoz surface passes through points (− 0.07,34,000), (− 0.03,518,000), (034,000), (0.035,50,000), and (0.0734,000). Therefore, the curve equation is

$$p = 17777\sin(44.857y) + 34000 \tag{12}$$

The non-uniform inflow II is distributed on the yoz section with curve passing points (− 0.07,30,000), (034,000), and (0.0738,000). Therefore, the curve equation is

$$p = 57142.857y + 34000 \tag{13}$$

The corresponding formulas were compiled into Fluent through UDF for subsequent numerical simulation. The pressure cloud diagram in Fig. 7 is a simulation of different pressure distributions in the pump inlet section using formulas 12 and 13. The pressure distribution of inlet section of inhomogeneous flow I in yoz section is a sinusoidal curve, and the hump in positive direction of y axis points to the inlet of the impeller, while the hump in negative direction of y axis points to the inlet of the impeller. The pressure distribution of the inlet section of inhomogeneous inlet flow II is linear, symmetrical with respect to yoz along the axis, gradually increasing in the positive direction and decreasing in the negative direction along the y direction. In order to make the flow in the impeller domain fully affected by the inhomogeneous flow, a straight pipe is

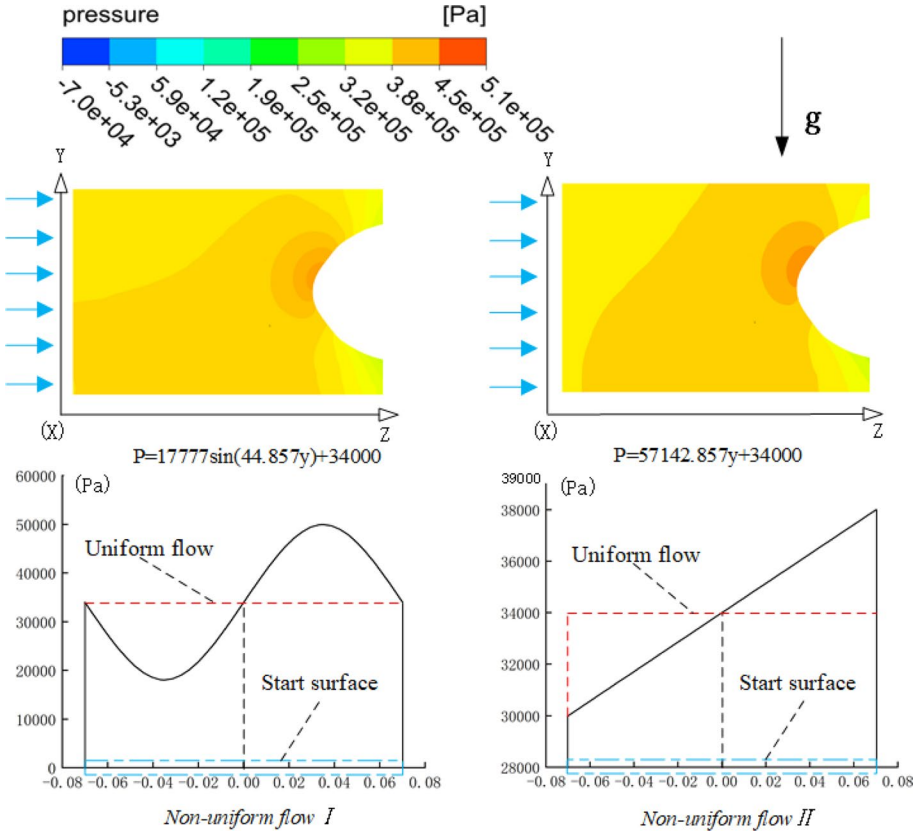

Fig. 7 Two types of heterogeneous inlet section pressure distribution diagram

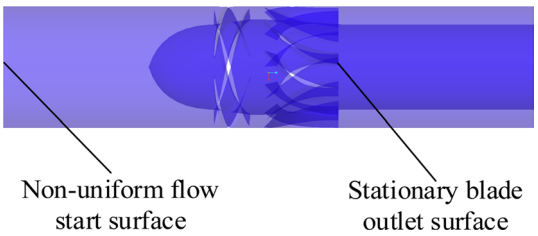

Fig. 8 Non-uniform inflow start surface

added in front of the inlet of the impeller. Figure 8 shows the final fluid domain and the starting surface of the non-uniform incoming flow.

6 Evolution process of performance failure caused by gas blocking

6.1 Bubble generation and evolution process in helical–axial flow multiphase mixed-transport pump

Figure 9 shows the visualization of bubble distribution and the simulation of bubble distribution at different times of the two non-uniform inflow flows. Three moments from critical cavitation to complete cavitation (T1 bubble birth, T2 bubble development, and T3 gas blocking) are, respectively, taken to analyze the gas–liquid separation development and activation process after cavitation.

As shown in Fig. 9, it can be seen that when bubbles are first generated at T1, the gas mainly appears in the impeller flow channel, and there are almost no bubbles generated in the diffuser flow channel. At this time, the forms of bubbles are mainly uniform bubbly flow and separated flow on the blade leading edge surface. At T2, as the flow develops, bubbles significantly increase throughout the entire flow channel. The separation flow at the leading and trailing edges of the blade continues to extend, and bubbles begin to aggregate and form a bubble like flow at the junction of the moving and stationary blade, with a local gas volume fraction of 100%. The gas inside the impeller also spreads through the diffuser channel, resulting in a large amount of uniform bubbly flow in the diffuser channel. At this time, the gas–liquid two-phase flow pattern in the impeller channel transitions from aggregated bubbly to gas blocking. At the final T3 moment, the bubbles fill the entire impeller channel, and the separated flow continues to extend; there is more aggregated bubbly flow at the junction of moving and stationary blade. Due to the pressure difference in the flow around the diffuser surface, the separated flow spreads from the leading edge of the diffuser pressure surface, and

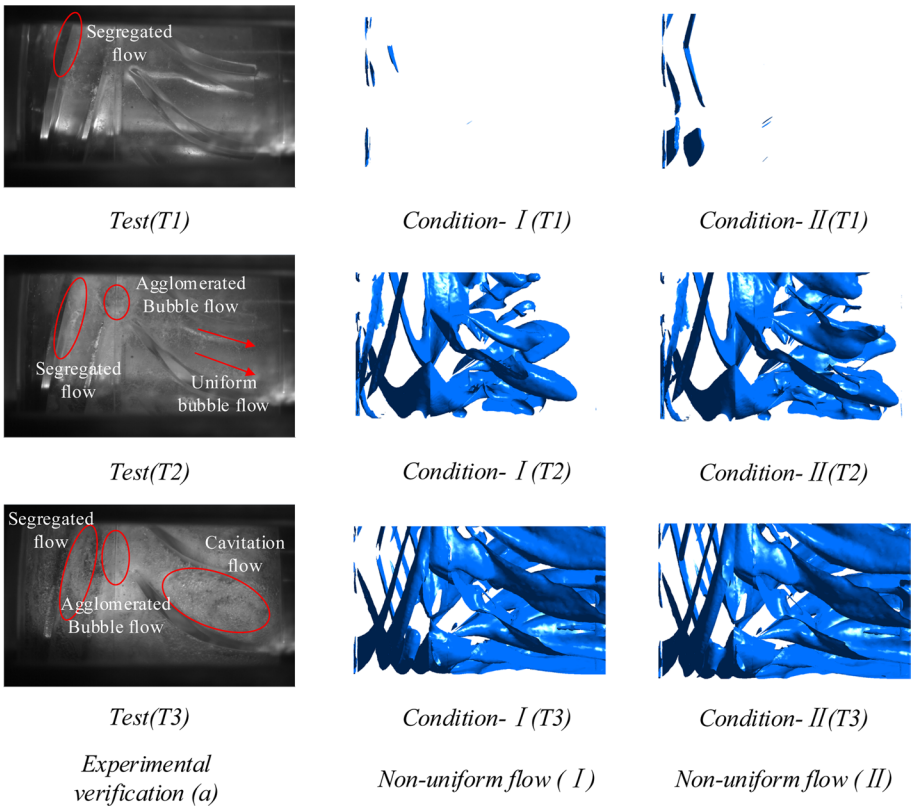

Fig. 9 Comparison of bubble evolution in experiments and simulations

the interaction with the separated flow at the trailing edge of the adjacent diffuser suction surface in the same flow channel blocks the flow channel.

6.2 Performance failure caused by gas blocking in helical–axial flow multiphase mixed-transport pump

According to Sect. 5 of this article, it can be seen that the programmed control of the inlet of the helical–axial multiphase mixed-transport pump during numerical simulation results in two specific inlet boundary conditions, which can effectively simulate the process of non-uniform flow causing bubbles to develop into air masses and block the flow channel. Figure 10 shows the head variation curve of a numerical simulation helical–axial multiphase mixed-transport pump. Compared with numerical simulation under pure water conditions, the head under both non-uniform inflow conditions shows a decreasing trend. When two non-uniform boundary conditions are applied, the head curve of the pump decreases with the increase in flow rate. At point a–a1, the bubbles form a bubbly flow in the impeller channel, and the head curve does not decrease significantly. As the flow rate increases, bubbles at point b–b1 fill the flow channel with

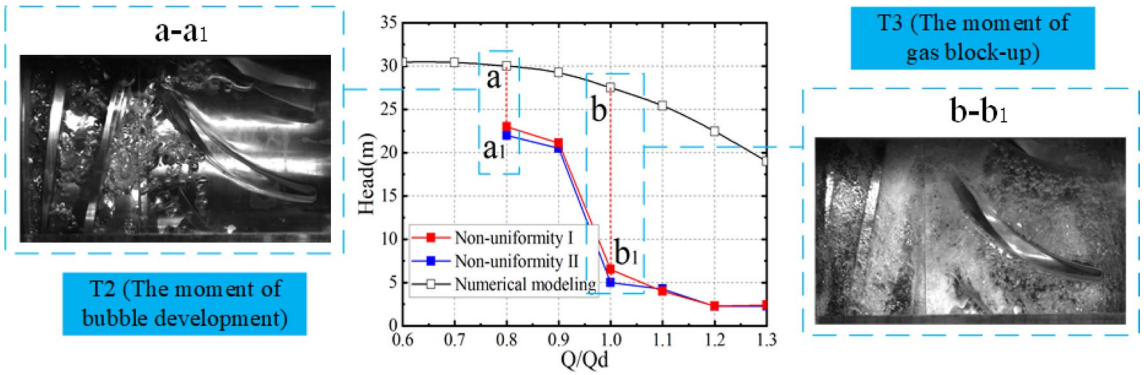

Fig. 10 Pump head curve when air blockage occurs

aggregated bubbly flow. From the head curve, it can be seen that the head of the pump decreases in a fractured manner, resulting in severe performance failure.

Analyzing Figs. 9 and 10, it is found that non-uniform inflows I and II can accurately simulate the evolution of bubbles at T1 bubble initiation and T3 gas generation blockage, and the proportion of non-uniform inflow II is longer when separated flow occurs on the blade surface. However, during the bubble development process of T2 (moment of bubble development) T3 (moment of gas blocking) a–a1, b–b1, non-uniform I and II have different effects on the intensification of bubbles in the flow channel. The separation flow on the blade surface is basically the same for both; with the development of bubbles, the interaction between bubbles occurs earlier and more prominent in non-uniform II, which is consistent with the visual experimental comparison. From this, it can be seen that the non-uniform II has a more pronounced effect on bubble activation in the flow channel under the two simulated specific inlet conditions.

7 Effect of different inflow conditions on performance failure caused by gas blockin

7.1 Setting of monitoring points

In order to study the velocity and pressure perturbations of impeller passage and inlet and outlet under two non-uniform inlet and outlet conditions when gas blockage occurs. In the process of gas blocking, the bubble clusters are mainly located in the middle of the flow channel, so monitoring points are set on the 0.5-span surface of the impeller and guide vane, respectively, for monitoring. As shown in Fig. 11, the axial length of the flow channel $L = 138$ mm, and the Y-axis direction is the expansion diagram of the flow channel with a cross section. Among them, five dynamic monitoring points yt1–yt5 are set on the convex surface of the impeller along the flow direction, and five dynamic monitoring points ya1–ya5 are set on the concave surface along the flow direction. Four static monitoring points dt1–dt5 are set along the flow direction on the convex surface of the guide vane. Four static monitoring points da1–da5 are set along the flow direction on the concave surface.

Among them, five dynamic monitoring points yt1–yt5 are set along the flow direction on the suction surface of the impeller, and five dynamic monitoring points ya1–ya5 are set along the flow direction on the pressure surface. Set four static monitoring points dt1–dt5 along the flow direction on the suction surface of the diffuser; four monitoring points da1–da5 are set along the flow direction on the pressure surface.

7.2 Changes in blade surface velocity at the onset of bubbles

Figures 12 and 13 show the variation of blade surface velocity along the flow channel under different flow conditions during bubble initiation under non-uniform inflow conditions I and II, respectively.

From Fig. 12, it can be seen that along the flow direction, the velocity at the monitoring point on the pressure surface of the impeller blade shows a phenomenon of first increasing and then slowly decreasing. It reaches its maximum at the monitoring point ya5 at the trailing edge of the blade, and reaches its minimum when transitioning from the middle section of the moving and stationary blade to the inlet da1 of the diffuser, because there is energy loss in the middle

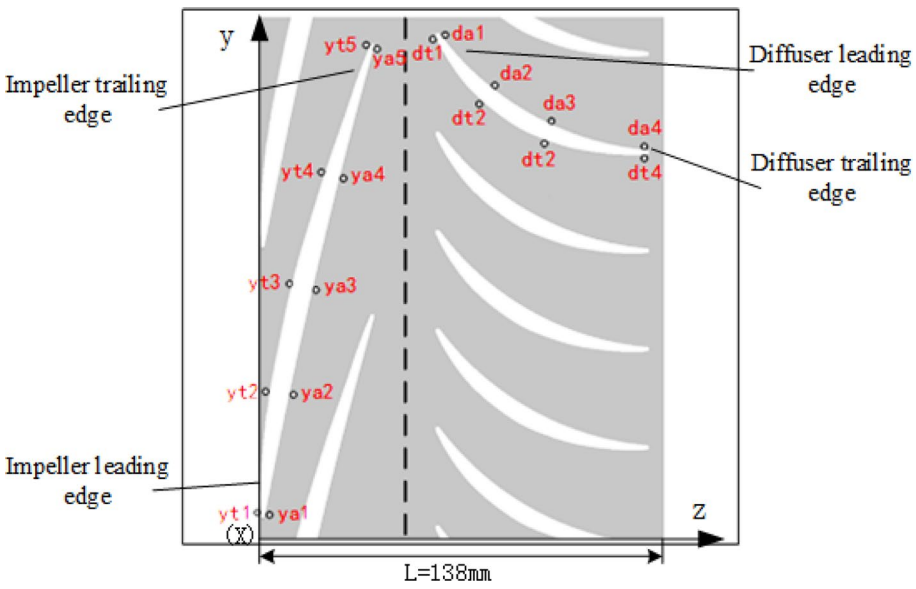

Fig. 11 Distribution of monitoring points

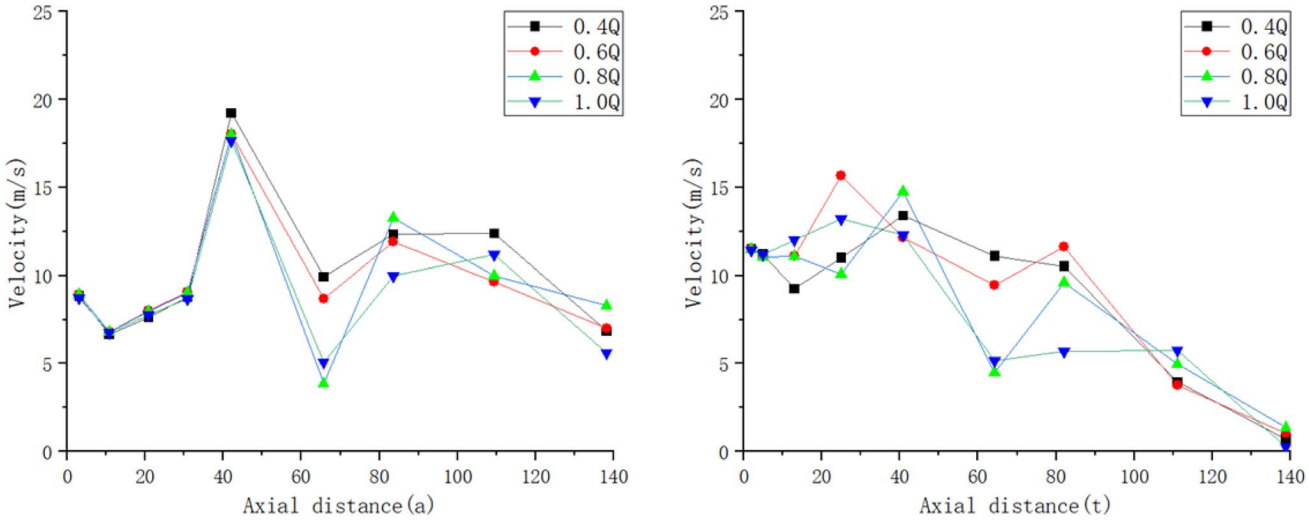

Fig. 12 Non-uniform I velocity of the blade surface at the beginning of bubbles

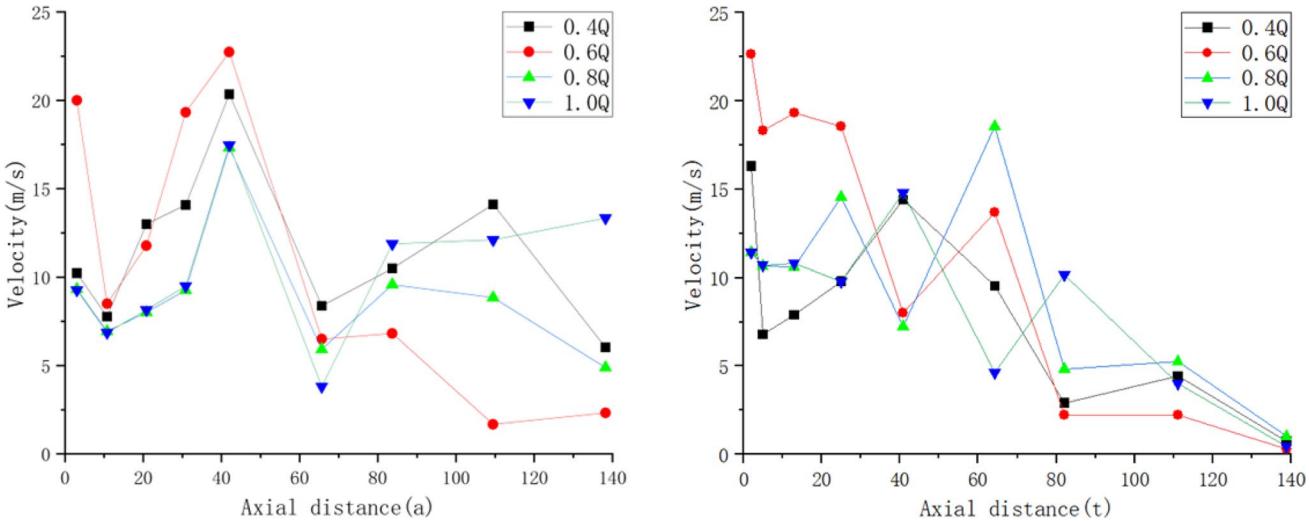

Fig. 13 Non-uniform II velocity of the blade surface at the beginning of bubbles

section. The variation is not significant with different flow conditions. In the flow direction, the velocity change at the monitoring points on the suction surface of the blade is relatively stable, in a parabolic form.

From Fig. 13, it can be seen that along the flow direction, the speed at the monitoring point on the pressure surface of the blade also shows a phenomenon of first increasing and then slowly decreasing, but the speed fluctuation at the inlet and outlet ends of the blade is relatively large under different flow conditions. The speed variation along the flow direction on the suction surface of the blade is relatively large, manifested as rising first and then stabilizing. The speed variation at the intersection of the moving and stationary blade under different working conditions fluctuates greatly. From this, it can be seen that the change in velocity at the beginning of bubble formation mainly occurs at the intersection of the pressure surface of the blade and the moving and stationary blade. The non-uniform inlet flow changes the velocity field of the impeller, while the high-speed rotating impeller perturbs the non-uniform inlet flow. The combination of the two effects ultimately leads to the development of gas blocking.

7.3 The distribution of blade surface pressure during the development of gas blocking

Analyzing Fig. 14, it can be observed that the pressure data changes on the pressure surface of the blade observed along the flow direction show that both non-uniform I and non-uniform II pressures first slowly decrease and then rapidly increase. Reaching the trough near point yo5 and reaching

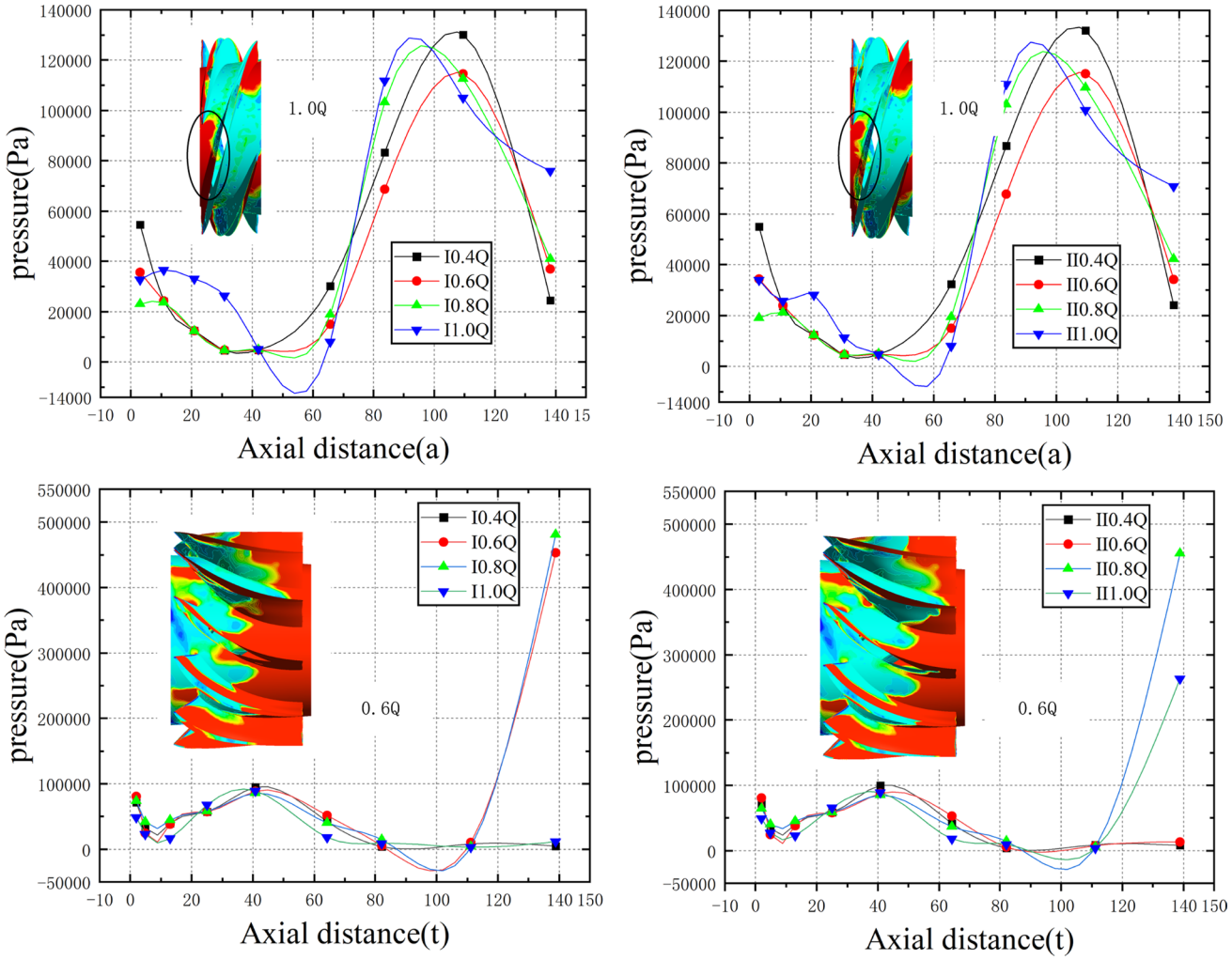

Fig. 14 Non-uniform pressure distribution of blade monitoring points under different working conditions

the peak near point do3 presents a horizontally placed S with a difference of 12 kPa between the maximum and minimum pressures. As the flow rate increases, the high-pressure points move to the left in sequence. However, as shown in Fig. 14, under the two conditions of 1.0Q, the pressure changes at points yo1–yo3 are relatively large. The pressure cloud map of non-uniform I is uniform, while the pressure cloud map of non-uniform II is more chaotic, ultimately leading to flow intensification and more obvious gas blocking phenomenon.

Along the flow direction on the suction surface of the blade, the pressure near point yt1–dt2 is basically maintained at around 0–10 kPa; the changes in pressure within this range also take the form of first decreasing, then increasing, and then decreasing. The trough appears near yt2 point, and the peak appears near yo5 point. From Fig. 14, it can be seen that there is a sudden increase in pressure within the range of dt3–dt4 points, with non-uniform I appearing at low flow conditions and non-uniform II appearing at high-flow conditions. From the pressure cloud map of 0.6Q, it can be seen that the high-pressure zone of non-uniform I near the diffuser outlet covers a wider range than that of non-uniform II.

8 Conclusion

This article integrates numerical simulation with visualization experiments to abstract incoming flow conditions using UDF. It delves into the phenomenon of non-uniform incoming flow, which triggers bubble activation, ultimately culminating in gas blocking within the flow channel of a helical–axial multiphase mixed-transport pump. In the future, we aspire to present a comprehensive model of this boundary condition from a systemic perspective, applicable to similar research endeavors. We aim for a harmonious integration of numerical simulation and experimental research, enabling computer science to effectively

serve engineering practice. The conclusions derived from this study are outlined as follows:

1. During the bubble evolution phase, bubbles that are subjected to linearly varying boundary conditions demonstrate more intense gas–liquid turbulence within the flow passage, prompting interactions between bubbles to occur at an earlier stage. Throughout this phase of bubble development, there is a notable 25% reduction in the head generated by the mixed-transport pump, a decrease that proves detrimental to the pump's efficient performance. This reduction in pump head significantly impacts the operational effectiveness, signaling a need for optimization in handling such dynamic gas–liquid mixtures.
2. At bubble initiation, velocity shifts on the pressure surface, induced by both sine and linear transformations, converge notably at the juncture of the moving and stationary blade. The velocity surges to its zenith of 22 m/s at the impeller's trailing edge. On the flip side, the suction surface undergoes marked velocity fluctuations amidst linear transformation. The linear transformation sets off a 5% velocity variation within the impeller's velocity field, which, when juxtaposed with the sinusoidal transformation, portrays distinct dynamic behavior. Concurrently, the briskly rotating impeller provokes disturbances in the non-uniform inflow, leading to an intertwined effect of both transformations on the system.
3. When gas blocking arises, the pressure on the pressure surface of the blade initially decreases before subsequently increasing. It reaches a nadir of − 10,000 Pa near the trailing edge of the impeller and peaks near the midpoint of the diffuser passage. Under high-flow conditions, pressure at the impeller inlet becomes more turbulent during linear transformation, causing the pressure on the suction surface of the blade to plummet to − 30,000 Pa within the middle range of the diffuser. Consequently, the head of the mixed-transport pump undergoes a rapid decline. It is recognized that the boundary conditions of linear transformation effectively emulate pressure fluctuations in the flow channel of a mixed-transport pump during gas blocking. This insight aids in the hydraulic design of the mixed-transport pump, ensuring its adaptability to more intricate incoming flow conditions.

Acknowledgements This work was partially supported by the National Natural Science Foundation of China (51969014), the Science Fund for Distinguished Young Scholars of Gansu Province (20JR10RA204), and Longyuan Youth and Fundamental Research Funds for the Universities of Gansu Province (2022LQGR51), with the Hongliu Outstanding Young Talents Funding Scheme of Lanzhou University of Technology

Declarations

Conflict of interest We declare that we have no conflict of interest.

References

1. Wang R, Wang L et al (2017) Research status of oil and gas mixed transport pumps [J]. Chem Manag 06:42–43 ((**In Chinese**))
2. Quan H, Sun J, Li Y et al (2023) Research on gas–liquid separation characteristics in the helico-axial multiphase pump [J]. Phys Fluid 35(11):1–14
3. Murakami M, Heya N (1966) Swirling flow in suction pipe of centrifugal pumps: 1st report, distribution of velocity and energy [J]. Bull JSME 9(34):328–337
4. Bhatti MM, Zeeshan A, Asif MA et al (2022) Non-uniform pumping flow model for the couple stress particle-fluid under magnetic effects [J]. Chem Eng Commun 209(8):1058–1069
5. Cao P, Wang Y, Kang C et al (2017) Investigation of the role of non-uniform suction flow in the performance of water-jet pump [J]. Ocean Eng 140:258–269
6. Luo X, Ye W, Huang R et al (2020) Numerical investigations of the energy performance and pressure fluctuations for a waterjet pump in a non-uniform inflow [J]. Renew Energy 153:1042–1052
7. Yuan Y, Fang Y, Tang L (2023) Effects of non-uniform elbow inflow on the unsteady flow and energy development characteristics of a centrifugal pump [J]. Phys Fluid 35(1):1–13
8. Xiaolong Z et al (2014) Prediction research on propeller hydrodynamic and noise characteristics in non-uniform [J]. Flow J Wuhan Univ Technol Transp Sci Eng 38(6):1300–1303
9. Liyun Liu et al (2020) a study on the flow field characteristics and noise mechanism of a non-uniform underwater propeller [c]. The fluid mechanics professional committee of the Chinese society of mechanics. In: Abstract of the 11th national conference on fluid mechanics. School of Aeronautics and Astronautics, Shanghai Jiao Tong University [C]
10. Huang R, Wang Y, Du T et al (2021) Mechanism analyses of the unsteady vortical cavitation behaviors for a waterjet pump in a non-uniform inflow [J]. Ocean Eng 233(108798):1–11
11. Jian D, Yude Y (2024) Effect of non-uniform incoming flow on the mixing enhancement in a scramjet cavity combustor [J]. Int J Hydrogen Energy 50:758–771
12. Zhang L (2013). Numerical simulation study for pressure fluctuation of axial-flow pump under non-uniform inflows [D] Yangzhou University (In Chinese)
13. Yokoyama B, Zhiying (1982) An Effect of water temperature on cavitation performance of centrifugal pump [J]. Huashui Technol Intell 10(01):128–134
14. Zhang H, Wang J, Zhang D et al (2021) Numerical analysis of the effect of cavitation on the tip leakage vortex in an axial-flow pump [J]. J Mar Sci Eng 9(7):1–21
15. Ali A, Si Q, Wang B et al (2022) Comparison of empirical models using experimental results of electrical submersible pump under two-phase flow: numerical and empirical model validation [J]. Phys Scr 97(6):065209
16. Yuan Z, Zhang Y, Zhang J et al (2021) Experimental studies of unsteady cavitation at the tongue of a pump-turbine in pump mode [J]. Renew Energ 177:1265–1281
17. Al-Obaidi AR, Qubian A (2022) Effect of outlet impeller diameter on performance prediction of centrifugal pump under single-phase and cavitation flow conditions [J]. Int J Nonlinear Sci Numer Simul 23(7–8):1203–1229
18. Al-Obaidi AR, Alhamid J (2023) Investigation of the main flow characteristics mechanism and flow dynamics within an axial flow

pump based on different transient load conditions [J]. Iran J Sci and Tech Trans Mech Eng 1:19
19. Al-Obaidi AR (2023) Effect of different guide vane configurations on flow field investigation and performances of an axial pump based on CFD analysis and vibration investigation [J]. Exp Tech 1:20
20. Penteado MRM, Vieira SC, de Castro MS et al (2022) Drift-flux model for gas–liquid flow subjected to centrifugal fields[J]. AIChE J 68(2):e17448
21. Wang C, Zhang Y, Zhu J et al (2021) Effect of cavitation and free-gas entrainment on the hydraulic performance of a centrifugal pump [J]. Proc Inst Mech Eng Part A: J Power Energy 235(3):440–453
22. Manninen M, Taivassalo V, Kallio S (1996) On the mixture model for multiphase flow [J]
23. Ansys I (2018) ANSYS fluent user's guide, release 19.0[J] ANSYS. Inc Canonsburg
24. Brennen CE (2014) Cavitation and bubble dynamics [M]. Cambridge University Press
25. Zwart P J, Gerber A G, Belamri T (2004) A two-phase flow model for predicting cavitation dynamics[C]. In: Fifth international conference on multiphase flow Yokohama Japan 152
26. Quan H, Yang X, Liu X et al (2023) Research on energy conversion characteristics in impeller of helical-axial multiphase pump during crude transportation [J]. Phys Fluid 35(2):1–11
27. Cui B, Lin Z, Zhu Z et al (2017) Influence of opening and closing process of ball valve on external performance and internal flow characteristics [J]. Exp Therm Fluid Sci 80:193–202